Research Article | Vol. 11, No. 6 / 1 June 2020 / Biomedical Optics Express 3346
Biomedical Optics EXPRESS

Tilt (in)variant lateral scan in oblique plane microscopy: a geometrical optics approach

MANISH KUMAR AND YEVGENIA KOZOROVITSKIY*

Department of Neurobiology, Northwestern University, Evanston, Illinois 60208, USA
yevgenia.kozorovitskiy@northwestern.edu

Abstract: Oblique plane microscopy (OPM) is a single objective light-sheet microscopy that performs three dimensional (3D) imaging by axial scan of the generated light-sheet. Recently, multiple techniques for lateral scanning of the generated light-sheet in OPM have emerged. However, their suitability for geometrically distortion free 3D imaging, which essentially requires a constant tilt light-sheet scan, has not been evaluated. In this work, we use a geometrical optics approach and derive analytical relationship for the amount of tilt variance in planar mirror based scanned oblique plane illumination (SOPi) arrangement. We experimentally validate the derived relationship and use it to arrive at an optimized scanner geometry and to understand its associated limitations. We discuss the effects of scanning on optical aberrations and 3D field of view in optimized, tilt invariant, lateral scanning OPM systems. We also provide experimental strategies enabling precise scanner alignment for tilt invariance, as well as an open source platform for rapid design of new oblique light-sheet microscopes.

1. Introduction

Light-sheet microscopy is a powerful imaging technique based on optical sectioning. The conventional light-sheet microscopy configuration consists of two objectives orthogonally arranged around a sample [1,2]. Several variants of light-sheet microscopy have been developed for more convenient sample access during imaging [3–8]. However, oblique plane microscopy (OPM) is a unique setup which performs light-sheet microscopy with a single objective facing a given sample, thus providing maximum steric access to the sample [9]. To achieve this, it combines the concepts of aberration free remote focusing and selective plane illumination microscopy (SPIM) [10–12]. In its original configuration, OPM performs 3D imaging by axial scan of the light-sheet, achieved by piezo mounted remote microscope objective [13,14]. The remote objective's axial movement results in an absolutely tilt invariant axial scan of the generated oblique light-sheet, making 3D reconstruction simple and free of geometrical distortions. Recently, multiple alternate scan configurations have been implemented in OPM for a more convenient, lateral scan of the generated light-sheet (see Fig. 1). Swept confocally-aligned planar excitation (SCAPE) microscopy was the first among these to introduce a polygon scan mirror based reflective arrangement, leading to lateral scan of the light-sheet [15]. A second configuration demonstrated oblique scanning two-photon light-sheet fluorescence microscopy (OS-2P-LSFM), which made use of a refractive transmission window for lateral scan of the light-sheet [16]. However, these scan arrangements were associated with several limitations. SCAPE introduced a scan position dependent tilt variation in the light-sheet, which is suboptimal for geometrical distortion free 3D imaging. The refractive window solution provided an absolutely tilt invariant scan for the excitation light-sheet, but not for the imaging path. Since this type of imaging relies on a relatively wide fluorescence spectrum, optical dispersion and aberrations (primarily spherical) are generated by a high refractive index glass window in the imaging path.

To combine the best features of the previous two arrangements, we introduced a plane mirror based scanned oblique plane illumination (SOPi) microscopy [17,18]. Our work focused on optical ray tracing simulations to obtain an optimized scan geometry to resolve the tilt variance

#389654 https://doi.org/10.1364/BOE.389654
Journal © 2020 Received 3 Feb 2020; revised 15 May 2020; accepted 18 May 2020; published 28 May 2020

Biomedical Optics EXPRESS

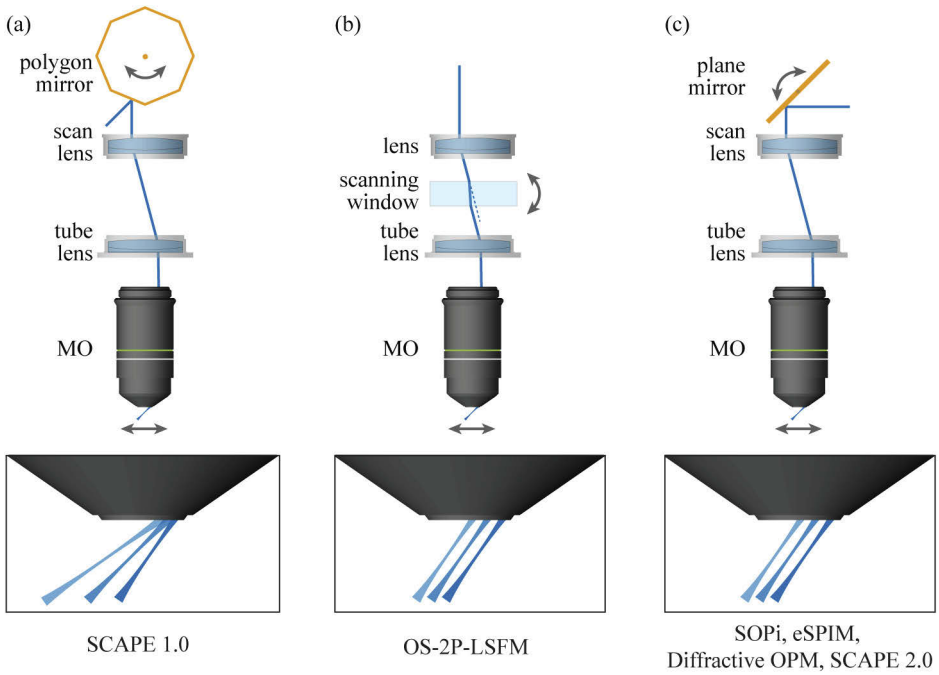

Fig. 1. Existing geometries for lateral scan of the generated light-sheet in OPM inspired systems. Insets show corresponding light-sheet scan orientations. (a) First arrangement uses a polygon mirror scanner to perform a lateral scan with varying tilt [15]. (b) Second arrangement uses a refractive transmission scanning window to perform constant tilt lateral scan [16]. (c) Third arrangement uses a plane mirror scanner to aim for constant tilt lateral scan [17–21]. MO: microscope objective.

problem for both scanned illumination and descanned signal rays. Here, a plane mirror scanner is placed with its rotation axis at the intersection of the back focal plane (BFP) and the principal axis of the scan lens. In parallel, Yang *et al.* independently introduced epi-illumination SPIM (eSPIM) with a plane mirror scanner for lateral scanning of the light-sheet [19]. However, eSPIM focused on solving the low effective numerical aperture (NA) issue of the OPM systems, and it did not delve into the scanner geometry. Subsequently, there has been a steady rise in the popularity of plane mirror scan geometry for creating systems with direct application in developmental biology and neuroscience. Two notable implementations include diffractive OPM and SCAPE 2.0 [20,21]. Diffractive OPM performs single objective light-sheet imaging with low NA objectives and results in a very large field of view imaging in small organisms. SCAPE 2.0 demonstrates the rapid imaging capability of lateral scan architecture in OPM by imaging unrestricted small organisms at cellular resolution.

Given the challenges of the first two scan geometries in Fig. 1, the plane mirror scan geometry is poised to become the preferred arrangement in future developments in this family of imaging techniques. However, plane mirror scanner geometry has not yet been studied in sufficient detail, in order to understand the underlying principles and, most importantly, the limitations of this scan geometry in OPM. Here, we perform a detailed geometrical analysis of this scan arrangement. We derive a relationship for evaluating tilt variance in a scanned light-sheet. We also perform an experiment to measure the actual variation in the tilt of an oblique beam and cross validate the derived relationship. We then use the derived relationship to arrive at an optimized scanner placement. In addition to addressing tilt invariance in oblique light-sheet scanning, we also evaluate optical aberrations and field of view in the optimized system during a lateral scan.

Biomedical Optics EXPRESS

2. Geometrical investigations of tilt invariant lateral scan and imaging

Geometrical optics is a simple yet powerful tool for analyzing optical systems. These intuitive analyses describe light as optical rays which travel in straight lines, bending or reflecting at interfaces, governed by well-known laws of refraction and reflection. Geometrical analysis is capable of investigating imaging performance and aberrations in an optical system [22]. Various ray tracing software, which are industry and research standards for optical system design and optimization, rely on concepts from geometrical optics [23]. In our earlier work, we performed ray tracing based optimization for arriving at the SOPi arrangement [17]. It remains unknown whether the scan is absolutely tilt invariant, and if not, its deviation from expected ideal behavior. Therefore, in this section we build a thorough geometrical analysis of the plane mirror based scanner, aimed towards tilt invariant scan through an optical lens. We analyze the behavior of optical rays in a single plane first, as their extension into a light-sheet configuration is straightforward.

2.1. Optical lenses, Fourier transform, and tilt invariant lateral scan

An optical lens is well known to behave as a Fourier transforming element [24]. In first-order representation, a point source placed on the BFP of an optical lens provides a set of collimated optical rays. As shown in Fig. 2(a), a point source offset by distance y leads to collimated optical rays with tilt angle α. In other words, if an optical ray emerges from a lens with a known tilt α, it can be uniquely associated with an offset point R on the BFP which is $y = f \times \tan\alpha$ distance apart from the principal axis, where f is the focal length of the lens. This property of an optical lens can be built upon to describe an ideal tilt invariant scan. This is also true for compound lenses, *e.g.* microscope objectives. In fact compound lenses, having compensated for optical aberrations, perform better than singlet lenses. Let us consider a planar mirror scanner placed with its rotation axis at R (on the BFP) as shown in Fig. 2(b). A laser beam hits the scanner at R, to get reflected towards the lens. Since the pivot point of reflected ray is fixed at R (on the BFP), it leads to a constant tilt lateral scan beyond the lens. This tilt angle $\alpha = \tan^{-1}(y/f)$ can be easily changed by shifting the scanner and hence the optical beam pivot point R along the BFP. For thin lenses under paraxial approximation, this reduces to a linear relationship

$$\alpha = \left(\frac{y}{f}\right), \tag{1}$$

where α is in radians. In practice, this linear dependence of tilt angle α on offset y is true for F-Theta scanning lenses as well as for flat-field lenses under long focal length, small offset limit.

2.2. Tilt invariant lateral scan and imaging

The geometry shown in Fig. 2(b) provides an absolutely tilt invariant scan of the oblique illumination beam. However, OPM is not limited to the consideration of excitation beam alone. It also requires consideration of the signal rays, arising due to optical scattering or emitted fluorescence from the sample. Unlike the excitation beam, signal rays in OPM are not confined to a particular tilt angle. Therefore, we need an optical scanner which provides tilt invariant scanning/descanning for a wide range of beam offsets. Figure 2(c) shows the SOPi arrangement under consideration for this task. An infinity corrected microscope objective serves as a Fourier transforming scan lens, and a plane mirror with its rotation axis at the intersection of the BFP and the principal axis operates as a scanner. A beam (blue line) with offset y forms an oblique illumination beam, and signal optical rays (green dotted) emerge at various tilt angles, where each tilt angle corresponds to a unique offset value y_1, y_2, y_3, etc. What remains to be determined is how the beam offset and therefore tilt angle of the optical rays change during scanning. Tilt variance in oblique optical beam would lead to distorted 3D scan of the sample, while beam offset dependent tilt variance would cause additional optical aberrations [23].

Biomedical Optics EXPRESS

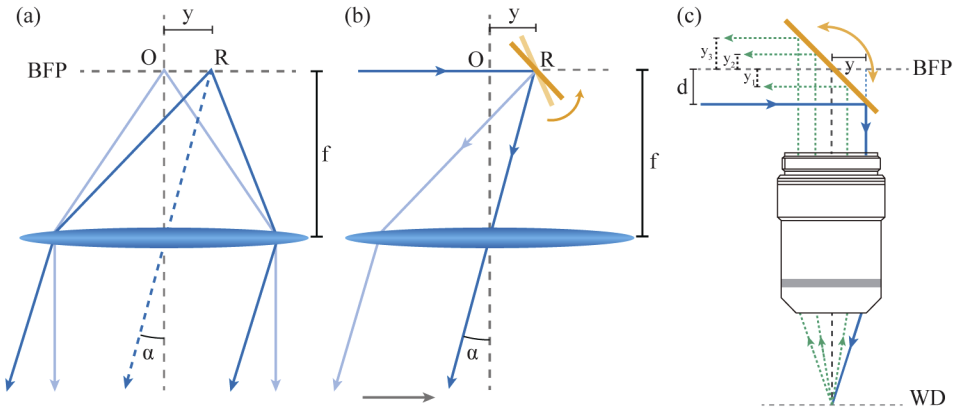

Fig. 2. Lens as an optical Fourier transforming element for tilt invariant scan and imaging. (a) A point source at the BFP leads to collimated optical rays where the lateral offset location of point source determines tilt angle of collimated rays. (b) A mirror scanner centered at the BFP leads to an absolutely tilt invariant lateral scan. (c) SOPi scan geometry under consideration for tilt invariant scan and imaging. WD: working distance.

2.3. Geometrical derivation

In this section we derive the relationship for scan dynamics of an optical beam in the SOPi geometry (Fig. 2(c)). For a generalized approach, we consider a scan geometry where the rotation axis of the scanner O is offset by d_y and d_z lengths along y and z axis, respectively. Figure 3 shows the magnified geometrical optics picture of this arrangement. OL and KL represent the horizontal and vertical offsets of scanner rotation axis from the intersection point of the principal axis and the BFP, respectively. Thus, $OL = d_y$ and $KL = d_z$. An optical ray MN is incident parallel to the BFP with an offset d from the scanner rotation axis O. This ray crosses the principal axis at M and hits the 45° tilted scan mirror (light orange) at P to get reflected vertically downwards along the z axis. When extended, the reflected beam meets the BFP at R. Thus, $ON \perp NP$, $NP \perp PR$, $KM = PR = d + d_z$, and $ON = LM = NP = d$. We now consider a new scanner position (dark orange) with the tilt angle $45° + \theta$. Following the laws of reflection, the optical ray now hits the scanner at Q and is reflected, making an angle 2θ with the z axis. This reflected optical ray, when traced backwards, meets the BFP at S. T is the intersection point of both reflected rays where $\angle PTQ = \angle RTS = 2\theta$. For an ideal scanner geometry, R and S should overlap, leading to a constant offset and hence an absolutely tilt invariant scan. However, in practice, the gap RS dictates the error, or tilt variance, during the scan.

In ΔONQ we have $\tan(\angle NOQ) = NQ/ON = (NP + PQ)/ON = 1 + PQ/d$. Therefore, $PQ = d \times (\tan(\angle NOQ) - 1) = d \times (\tan(45° + \theta) - 1) = d \times [(1 + \tan\theta)/(1 - \tan\theta) - 1]$.

Or,

$$PQ = \frac{2d \times \tan\theta}{1 - \tan\theta}. \tag{2}$$

In ΔTPQ we have $\tan(\angle PTQ) = PQ/PT = PQ/(PR - RT) = PQ/(d + d_z - RT)$. Therefore, $RT = d + d_z - PQ/\tan(\angle PTQ) = d + d_z - PQ/\tan(2\theta)$. Replacing PQ from Eq. (2) and expanding $\tan(2\theta)$ we get $RT = d + d_z - d \times (1 + \tan\theta)$. Or,

$$RT = d_z - d \times \tan\theta. \tag{3}$$

In ΔTRS we have $RS = RT \times \tan(\angle RTS)$. Or,

$$RS = (d_z - d \times \tan\theta) \times \tan(2\theta), \tag{4}$$

Biomedical Optics EXPRESS

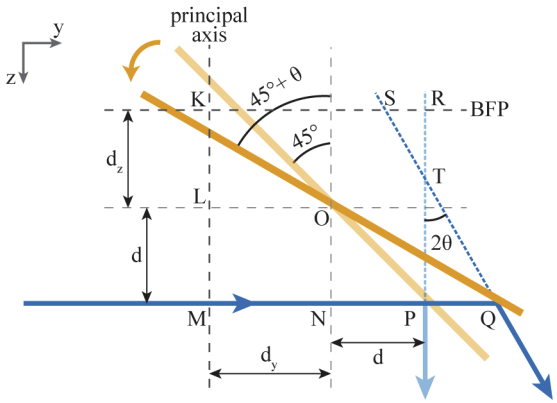

Fig. 3. A generalized SOPi scan geometry for the evaluation of tilt variance. Principal axis: optical axis of the microscope objective (objective not shown); O: rotation axis of the scanner; d_y: lateral offset of the scanner from the principal axis; d_z: axial offset of the scanner from the BFP; d: offset of the incident beam from the scanner rotation axis; θ: tilt angle deviation of the scan mirror.

where we replaced RT from Eq. (3). Here, we can use RS to precisely calculate tilt variance in the oblique optical beam during scan. The practical value of scan angle is θ<5°, implying that RS is smaller than d_z. Moreover, scanning lenses have much longer focal lengths, compared to beam offsets and scanner position offsets (*e.g.* Ref. [18] used f = 100 mm and offset d = 3.54 mm). Therefore, we have $KR/f = (d + d_y)/f \ll 1$ and $KS/f = (d + d_y - RS)/f \ll 1$. This makes the small angle approximation valid and we can use Eq. (1) to express tilt variance in an optical beam as $\delta = [\alpha_0 - \alpha_\theta] = [(KR/f) - (KS/f)] = RS/f$, where α_0 and α_θ correspond to 45° and (45° + θ) mirror tilt angles, respectively. Replacing RS from Eq. (4) we have

$$\delta = \left[\frac{d_z \times \tan(2\theta)}{f} - \frac{d \times \tan(\theta) \times \tan(2\theta)}{f}\right], \tag{5}$$

where δ is in radians.

Several considerations follow from Eq. (5). For a given practical value of tilt angle (θ<5°), the first term of the equation is at least one order of magnitude larger than the second term. This implies that d_z plays a greater role in tilt variance. On the other hand, the second term is responsible for beam offset dependent tilt variance, and it may lead to optical aberrations in the system. Notably, tilt variance of the system increases with scan angle θ. On a closer inspection of Eq. (5) (and Eq. (4)), it becomes clear that $d_z = (d \times \tan\theta)$ makes RS zero, leading to an absolutely tilt invariant scan. However, this relationship cannot be satisfied for a wide range of θ unless $d_z = d = 0$. This happens when both the incident beam and the rotation axis of the scanner are aligned to the BFP, *i.e.* the ideal scan condition as shown in Fig. 2(b). If θ is restricted to small values, a nonzero d is allowed when d_z approaches zero. This optimized case matches the schematic shown in Fig. 2(c), and is consistent with the previously published geometry of SOPi [17,18]. We can further conclude from the expression for RS that an offset along the lateral direction (d_y) does not change tilt variance in the system. However, a non-zero d_y would change overall tilt of the oblique beam (see Eq. (1)) and an off-axis placement of the scanner would make the imaging system asymmetric. Therefore, the optimal scanning arrangement is one with $d_y = d_z = 0$. Here, the tilt variance expression from Eq. (5) becomes $\delta \approx RS/f = -d/f \times \tan(\theta) \times \tan(2\theta)$. Note that δ is in radians here. Considering an extreme example with a large scan angle θ = 10°, a large offset d = 10 mm, and f = 100 mm, we get tilt variance $\delta \approx 0.37°$. This value of tilt variance is small for most practical purposes. However,

Biomedical Optics EXPRESS

based on subsequent optical elements, tilt variance can get magnified to become substantial. For example, the SOPi setup in Ref. [17] introduces 22.22× angular magnification, leading to effective ~ 8.2° tilt variance in the sample volume for the example case described above.

3. Experimental validation

Next, we performed an experimental validation of the derived tilt variance relationship. For this we needed a Fourier transforming lens, a plane mirror based scanner, and a method for measuring the beam tilt angle α. The schematics of the setup are shown in Fig. 4. We used a low magnification, long working distance microscope objective (4×, 0.1 NA, f = 50 mm, WD = 30 mm, Nikon) as a Fourier transforming lens. The advantage of using a low magnification objective, in addition to its long working distance allowing easy sensor placement, is that its BFP lies outside the body of the objective and is therefore directly accessible without the need for a pair of lenses to relay it to the scanner. A galvanometer mounted plane mirror (QS12, 10 mm aperture, Nutfield) served as the scanner. Since the precise placement of the galvo scanner was crucial, we first directed a collimated laser beam backwards through the microscope objective. This beam converged at the BFP of the objective, where the galvo scanner was carefully aligned to match the convergence point at the BFP with its rotation axis. We used a HeNe laser (HNL100L, Thorlabs) for both alignment and experiment. We used a neutral density filter (not shown in figure) to reduce the laser power and reflected the laser beam towards the galvo scanner using a mirror mounted on a manual translation stage. This precision translation stage helped in varying the offset d for the incident laser beam. We used a precision translation stage mounted camera as a tool for measuring the outgoing beam tilt α. As shown in Fig. 4(a), the camera sensor plane was oriented perpendicular to the principal axis, and it served to capture beam position at two predefined positions $\pm p$ distance away from the working distance of the microscope objective. This arrangement enabled the calculation of beam tilt

$$\alpha = \tan^{-1}\left(\frac{\Delta}{2p}\right) \approx \frac{\Delta}{2p},$$

where Δ is the absolute shift between the beam positions on the two planes (see inset Fig. 4(b)) and $\Delta \ll 2p$ invokes the small angle approximation leading to the relationship above. We used a camera with 3.45 μm pixel size (Blackfly, BFS-U3-16S2M-CS, FLIR) and p = 10 mm for our experiments. This arrangement has beam tilt measurement resolution of ~ 0.01°. Since beam divergence led to large beam size on camera, the center of each circular spot was noted as the beam position. As depicted in Fig. 4(b), the beam tilt measurements at two extreme scan points corresponding to galvanometer tilts θ_1 (for V_1 voltage) and θ_2 (for V_2 voltage) determined the tilt variance

$$\delta_{exp} = \alpha_2 - \alpha_1 = \frac{\Delta_2}{2p} - \frac{\Delta_1}{2p}, \tag{6}$$

where δ_{exp} is in radians. During experiments, a third precision translation stage (not shown in figure) helped shift the microscope objective and hence control d_z. Even with careful alignment of the camera linear translation stage, a slight angular mismatch in its translation axis and the microscope objective's principal axis is unavoidable. This mismatch gives rise to a consistent offset in the beam position, when measured at two camera positions. This offset is a constant value that can be easily compensated for by recording the on-axis beam positions (with d = 0 mm) at the two planes.

We performed experiments for d_z = 0 mm and d_z = 8 mm. For each of these cases, we recorded the beam positions on two planes ($2p$ = 20 mm apart), with two voltages $V_{1,2} = \pm 0.4$, and four offset values d = 0 mm, 1 mm, 2 mm, and 3 mm. For each of these combinations, we obtained Δ_1 and Δ_2 as displayed in the unit of pixels (px) in Table 1. We experimentally measured the galvanometer's tilt angle θ as ±0.92°, in response to the applied ±0.4 V. This was determined

Biomedical Optics EXPRESS

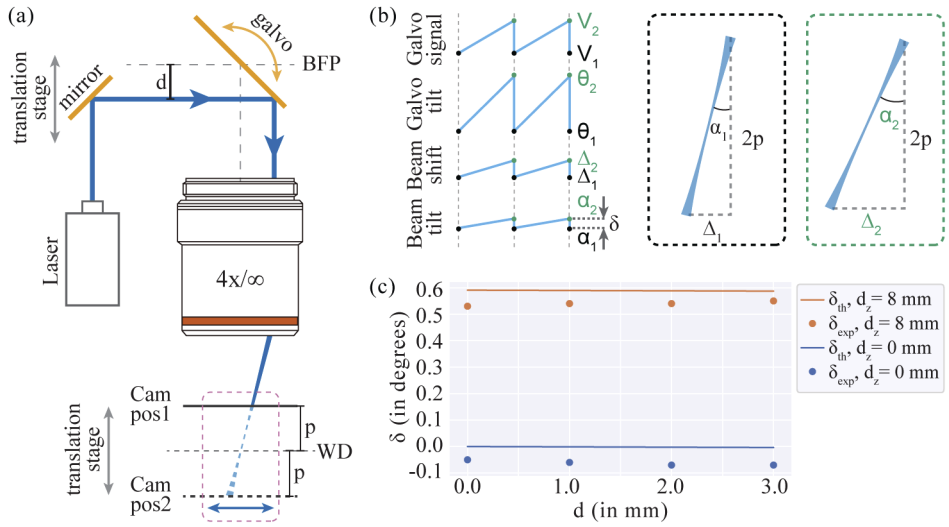

Fig. 4. Experimental strategy for evaluation of tilt variance. (a) Schematic of the experimental setup for measuring tilt variance. (b) Dependencies between voltage applied to galvo, galvo tilt, and beam shift/tilt. (c) Comparison of theoretically calculated and experimentally evaluated tilt variance for given galvo and beam offsets. The difference between theoretical and experimental values determines the error in galvo positioning.

by measuring the deflection in galvanometer reflected laser beam, propagating through air onto a distant screen, in response to the applied voltage and using $\theta = 0.5 \times \tan^{-1}(\textit{deflection} \div \textit{screen distance}) = 0.5 \times \tan^{-1}(\pm 2.4\,mm/74.5\,mm)$. Having confirmed that the small angle approximation is valid with our choice of parameters $d_z = 8$ mm, $d = 3$ mm and $f = 50$ mm, we used Eq. (5) to calculate δ_{th} values in Table 1. We filled in Δ_1 and Δ_2 values from the experimental measurements of beam positions and used Eq. (6) to calculate δ_{exp}. Figure 4(c) shows a plot of δ_{th} and δ_{exp}.

Table 1. Calculation of Tilt Variance During Scan

d_z (mm)	d (mm)	δ_{th}	Δ_1 (px)	Δ_2 (px)	δ_{exp}
0	0	0.00°	0	-5	−0.05°
0	1	0.00°	170	164	−0.06°
0	2	0.00°	244	237	−0.07°
0	3	0.00°	367	360	−0.07°
8	0	0.59°	-28	25	0.53°
8	1	0.59°	88	142	0.54°
8	2	0.59°	201	255	0.54°
8	3	0.59°	315	370	0.55°

It is evident from Table 1 and Fig. 4(c) that the theoretical and experimental values of tilt variances tightly match. Moreover, it is clear that tilt variance is mainly dependent on d_z and has negligible dependence on beam offset d. A closer inspection shows that δ_{exp} is consistently offset along one direction from δ_{th} (average offset = −0.06°). This consistent offset can be explained by an unintentional residual d_z remaining in the setup during galvanometer alignment. In fact, Eq. (5) translates −0.06° offset in δ into $-800\,\mu m$ offset in d_z. Therefore, we compensated galvanometer position by this length to obtain a perfect alignment for tilt invariant scan. This

Biomedical Optics EXPRESS

analysis highlights the following aspects of SOPi scanner geometry. First, the SOPi system is highly sensitive to galvanometer positioning. Second, even careful experimental alignment may not be precise enough to obtain tilt invariant scan. Third, measurement of tilt variance during scan, combined with our derived relationships, can be used for precise measurement and correction of galvanometer position. Fourth, tilt variance for the corrected system can approach zero, leading to a practically tilt invariant scan.

4. Optical aberrations and field of view during SOPi scanning

We have demonstrated that the SOPi scan geometry can offer tilt invariant scanning and imaging with an oblique light-sheet. However, it remains important to consider any limitations of this scan geometry. In this section we assess the effects of scanning on optical aberrations and field of view. We continue with a geometrical optics approach for these analyses.

4.1. Optical aberrations during scanning

Optical aberrations in a lens can be evaluated by tracing a pencil of parallel optical rays and observing how well they converge [23,25]. An unaberrated optical lens leads all of the parallel rays to converge to a single point. Any deviation from this behavior is credited to the presence of optical aberrations. To evaluate optical aberrations due to the previously described scan arrangement, we consider an optical aberrations free lens in the optimized scan geometry where $d_z = 0$. This leads to $RS = -d \times \tan\theta \times \tan(2\theta)$ (from Eq. (4)), and corresponding tilt variance $\delta = RS/f = -d/f \times \tan\theta \times \tan(2\theta)$ (from Eq. (5)). There remains a residual tilt variance term which is proportional to d. In other words, an optical ray undergoes different amount of tilt variance based on its offset position from the principal axis. At first, it appears that this beam offset-dependent tilt variance is similar to the spherical aberration term of an optical system and would lead to additional optical aberrations in the system [23]. If true, scanning would accumulate optical aberrations even if ideal lenses were used in this scanner arrangement. However, this is not the case. As clear from Fig. 5, a non zero tilted plane mirror causes a pencil of optical rays to get stretched (or compressed) along the lens aperture. Moreover, the magnitude of this stretch is proportional to the offset of individual rays. This stretching causes a change in tilt of the rays beyond the lens. Figure 5 shows that all optical rays, following the law of reflection, make a constant 2θ angle with the principal axis. This angle is independent of offset d. As a result, these rays perfectly converge to a point on the focal plane, $y = f \times (2\theta)$ away from the

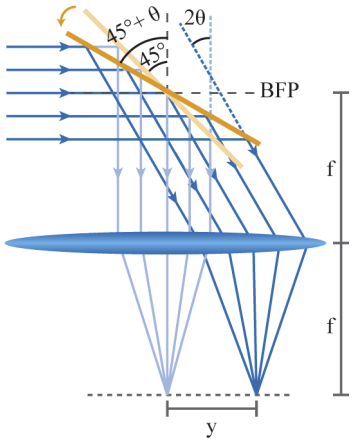

Fig. 5. Effect of lateral scanning on optical aberrations.

Biomedical Optics EXPRESS

principal axis, where 2θ is in radians. Therefore, a plane mirror scanner does not add any optical aberrations in this microscopy setup. In other words, optical aberrations in the setup are due to optical lenses and not scanner geometry. It is important to note that in practice, the off-axis imaging characteristics of optical lenses may place a limit on the achievable scan range.

4.2. Three dimensional field of view during scanning

So far we have seen that SOPi scanning arrangement provides tilt invariant lateral scan and adds no optical aberrations in the system. Next, we consider the field of view (FOV) characteristics of SOPi scanning arrangement. A microscope objective is designed for a particular FOV which, as illustrated in Fig. 6(a), is specified as a disk of certain diameter at the working distance of the objective. A point lying outside the FOV is not imaged sharply, due to clipping of a subset of optical rays, *i.e.* vignetting. SOPi and related systems perform 3D imaging, requiring a consideration of the 3D FOV. Moreover, even the 2D FOV of the system is unusual due to the oblique nature of the light-sheet, requiring careful consideration.

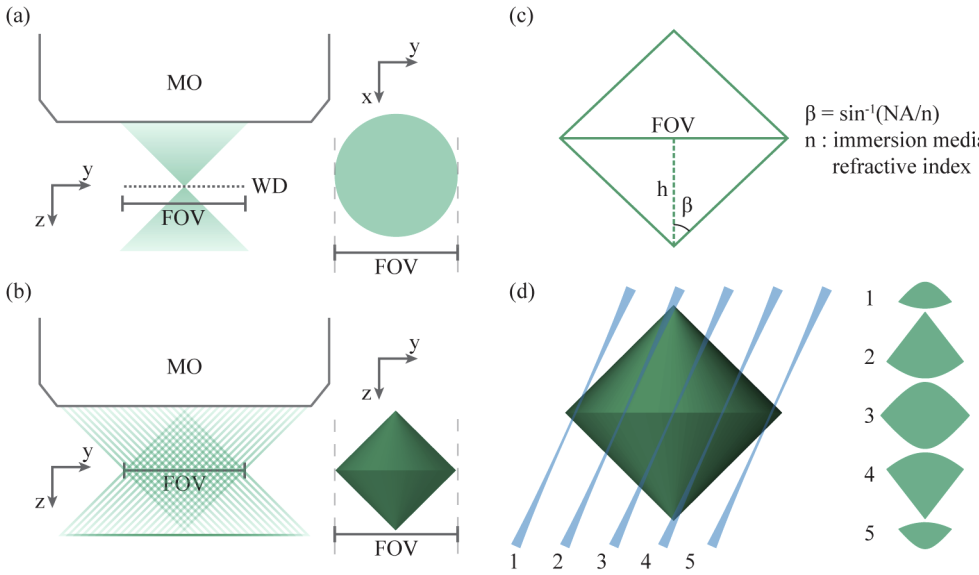

Fig. 6. 3D field of view in SOPi-like microscopy. (a) Acceptance cone of a microscope objective and corresponding two dimensional field of view. (b) A complete picture of acceptance cones through two dimensional field of view, where the overlapping region (double-cone shape) defines the three dimensional field of view. (c) Relationship between 2D field of view, NA, and 3D field of view. (d) Light-sheet orientation and corresponding cross-sectional field of view during lateral scan in SOPi microscopy (also see Visualization 1).

Figure 6(b) shows the set of all acceptance cones through the 2D FOV of the microscope objective. For illustration purposes, we have shown a cross section view with the edges of each cone and have made them equidistant within the region. Clearly, any point lying outside the crossed lines region will not get completely covered by the total acceptance cone angle of the objective. Therefore, the 3D FOV of the system is essentially a double cone shaped region as shown on the right in Fig. 6(b). In Fig. 6(c) we see that the double cone shape is made of two identical cones of height $FOV \div (2 \times \tan\beta)$ joined at their bases. Here, $\beta = sin^{-1}(NA/n)$ is the half acceptance angle of the imaging system. All points inside this double cone 3D FOV are imaged sharply by a SOPi-like microscope. At a given scan position, 2D FOV would be

Biomedical Optics EXPRESS

represented by the intersection of 3D FOV and the light-sheet plane. Thus, 2D FOV in SOPi microscopy varies with lateral scan position and tilt angle of the light-sheet, potentially limiting the overall system lateral scan range. Figure 6(d) and Visualization 1 show the effective 2D FOV of a SOPi-like microscopy at various lateral scan positions. It is apparent that the lateral scan range is large for thin samples and reduces with an increase in sample thickness (z-axis range) when imaging the full sample is desired.

Note that higher NA objectives increase the cone angle β and in turn lead to smaller oblique 2D FOV and 3D volume that can be imaged effectively. Nevertheless, the lateral scan range does not depend on the objective NA for a given FOV size. Thus, employing very high NA objectives results in enhanced resolution at the cost of reduced oblique 2D FOV, or sample thickness. For lower NA objectives, the attainable oblique 2D FOV and 3D volume grows due to increased imaging depth, at a cost of reduced lateral scan range. There is always a compromise between NA, sample thickness (oblique 2D FOV), and lateral scan range. Importantly, the overall effective NA of the microscopy system depends on the selection of the first microscope objective and subsequent optical elements, as described in appendix A and appendix B.

5. Conclusion

We have performed a detailed geometrical analysis of tilt variance in scanned oblique plane microscopy, derived the optimal layout analytically, developed an experimental method and performed a measurement of tilt variance in a specific low NA objective and scanner arrangement, with a generalized method applicable to higher NA objectives. These results confirm that essentially tilt invariant scanning can be achieved by lateral scan implementations of OPM inspired systems, but highlight the importance of precise scanner positioning and alignment for tilt variance and imaging performance control. Moreover, the experimental measurement of tilt variance, combined with our derived analytical relationship, can be used as a tool for precision alignment and positioning of scanners in these systems. We have also pointed out the absence of additional optical aberrations, important 3D FOV features, and lateral scan range constraints for this class of scanning arrangements. These analyses and strategies for attaining tilt invariant scanning, along with an open source GUI to facilitate new SOPi style microscope designs, create an opportunity for rapid adoption of oblique light-sheet techniques in bespoke systems optimized for a diverse range of neurobiological and biological sample types.

Appendix A: Extending tilt variance measurements to high NA SOPi systems

In section 3, we devised a practical strategy for easy alignment of a low NA setup with a long working distance 4x objective. Low magnification objectives have been shown to be useful in oblique plane microscopy [20]. However, multiple oblique plane microscopy arrangements rely on high NA, high magnification, small working distance objectives [17–19,21,26]. Figure 7(a) shows the schematics of such an arrangement. There are two major concerns when considering this complex setup: 1) how do the derivations for the simple scanner geometry, composed of a mirror and an optical lens, described in this manuscript, function in the full SOPi system; and 2) how to use the tilt variance measurement as a tool for alignment of microscopy systems with high NA, small working distance objectives?

To address the first question, let us start by simplifying the SOPi arrangement of Fig. 7(a). The SOPi arrangement includes three microscopy subsystems, each consisting of a microscope objective and a tube lens (Fig. 7(b)). The choice of the microscope objectives and the tube lenses determine the magnification of these subsystem modules (M1-M3). A 4F subsystem relays the image plane of the first microscopy module to the second one. The ratio of SL1 and SL2 focal lengths provides the magnification factor of the 4F system. A careful selection of these components allows the magnification factor of the 4F subsystem, M1 and M2, to satisfy Herschel's condition [17,22]. This enables a stigmatic re-imaging of the 3D volume in front of MO1 to a 3D

Biomedical Optics EXPRESS

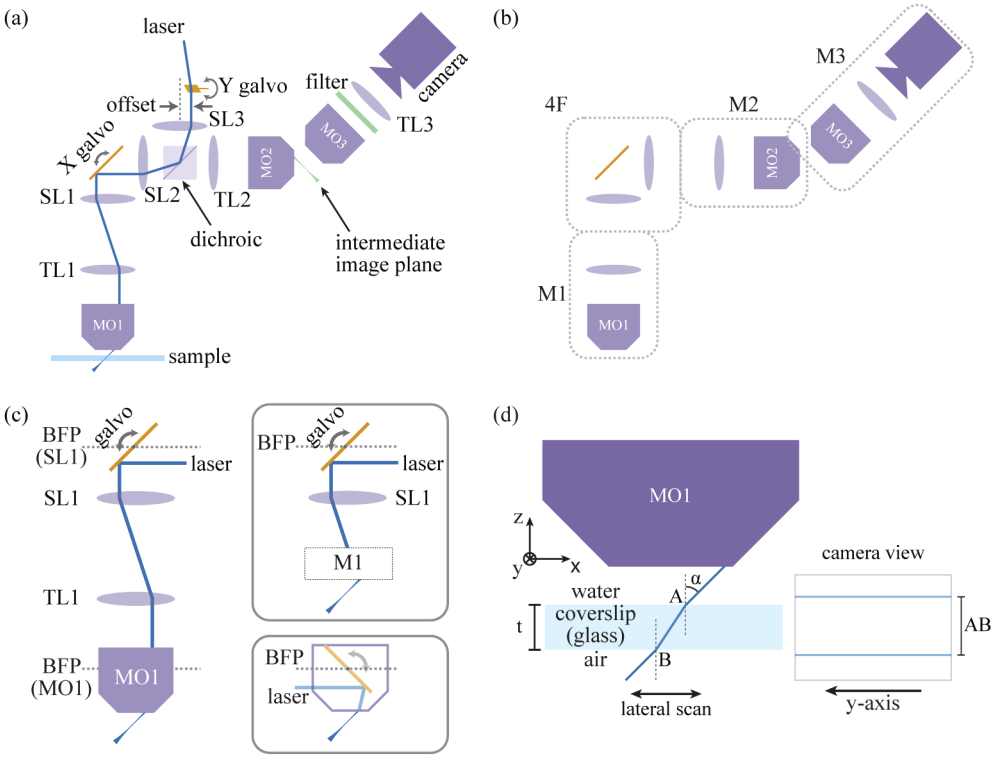

Fig. 7. Understanding tilt variance in high NA objective based SOPi microscopy. (a) Schematics of a standard SOPi microscopy system. (b) Subsystems of a SOPi arrangement. (c) Tilt invariant galvo-lens scanning subsystem in SOPi, and (d) measuring beam tilt in a high NA SOPi system. SL: scan lens, TL: tube lens, M: microscopy module, t: coverslip thickness, AB: coverslip oblique thickness.

volume in front of MO2. Thereafter, an independent alignment of the third microscopy module (M3) images any oblique section out of this 3D volume. We can now introduce the concept of tilt invariant scanning. For this we examine the first module and a half of the 4F subsystem, as presented in Fig. 7(c) (left), which we have considered throughout this manuscript. First, we can consider the MO1-TL1 pair together as a subsequent subsystem, with M1 linear demagnification (top inset box in Fig. 7(c)). The setup now reduces to a familiar galvo-lens scanner, followed by M1 angular magnification (and M1 linear demagnification). The second approach is to consider the SL1-TL1 lens pair together. It reimages the galvo scanner, while simultaneously scaling it by an associated magnification factor, to the BFP of MO1 (bottom inset box in Fig. 7(c)). Notice that, unlike for a 4x objective, the BFP of high NA, high magnification objective lies within the objective housing and is not directly accessible. Both lines of reasoning clarify galvo-lens scanning in the context of high NA objective based SOPi microscopy. It now follows that a plane mirror-based galvo scanner can give rise to tilt invariant lateral scanning. The remaining half of the 4F system relay, along with the second microscopy module (M2), completes the stigmatic re-imaging of the optically sectioned oblique plane, while the last microscopy module (M3) magnifies this plane to form the final image on a camera.

Next, we lay out a method for tilt variance measurement with high NA, small working distance objectives. The experimental strategy presented in section 3 uses the measurement of beam position at two distances in front of the objective, which is simple to perform with a long working distance 4x objective. However, higher NA objectives come with a few millimeter working

Biomedical Optics EXPRESS

distance at best, posing challenges for beam tilt measurement. Figure 7(d) shows an inexpensive and accessible solution to this problem, by placing a coverslip, as our sample of interest, in front of the main objective and imaging it on the SOPi system. The camera would show clear images of the illuminated water-glass (assuming MO1 is a water immersion objective) and glass-air interfaces of the coverslip. The oblique thickness of the coverslip (AB) reports the beam tilt in the setup. A constant beam tilt during scanning results in constant length AB. The knowledge of coverslip thickness t and its refractive index n_g allows for an easy calculation of the actual beam tilt $\alpha = \sin^{-1}[(n_g/n_i) \times \sin(\cos^{-1}(t/AB))]$, where n_i is the refractive index of the immersion media placed between the microscope objective and the coverslip. If weak optical scattering from the coverslip interfaces is not visible, the addition of a fluorescent dye (or beads) coating would solve this problem.

Appendix B: Designing your own single objective light-sheet microscope

Single objective light sheet microscopy, through its various adaptations, is rapidly evolving for applications to a broad range of specimens [9,13–21,26]. Although we have provided a detailed analysis and systematic breakdown of the entire microscopy system, it is not trivial to design a new one from the bottom up. The choice of various optical components, physical conditions, and system parameters are interconnected. To address this problem for the field, we present an open source tool called *Crossbill Design*.

Crossbill Design includes a friendly graphical user interface (GUI) to help a user design single objective light-sheet configurations in a systematic manner. It is written in Python and is platform-independent. The code along with a complete set of instructions on how to run it is freely available on zenodo [27]. A snapshot of the GUI is shown in Fig. 8. The acronyms used in the GUI are the same as in Fig. 7(a). The rightmost column of the GUI has clickable buttons to register the entered or selected values from the corresponding row. The text box below each button displays results corresponding to the user's selection and guides users on how to proceed. Listed below is a standard design routine:

- Select MO1 and MO2 parameters. Here the first two objectives can be chosen from a drop down menu. Magnification selection (or entry) can be made through an editable drop down list. The numerical apertures and immersion media refractive indices of the objectives can directly be entered in the corresponding text boxes.
- Click the first button to register MO1 and MO2 parameters. The corresponding text output box confirms the registered values, points out the NA limiting objective, reports the maximum achievable light-sheet tilt angle in the sample, and guides the user on how to choose values in the following steps to satisfy Herschel's condition for minimal aberrations.
- Enter tube lens and scan lens focal lengths in the text boxes. These values determine the magnification factor of the 4F system, microscopy modules M1 and M2 (see Fig. 7(b)).
- Click the second button to register the entered parameters. The corresponding text output box confirms the registered values and points out whether Herschel's condition is satisfied.
- Select or enter MO3 parameters, followed by TL3 and camera parameters.
- Click the third button to register the entered parameters. The corresponding text output box confirms the registers values and reports maximum system NA (along both major and minor axes of the effective NA ellipse), system magnification, camera limited 2D field of view, and whether Nyquist sampling is satisfied.
- Enter SL3 focal length, desirable light-sheet tilt angle in the sample, and field numbers for all three objectives.

Biomedical Optics EXPRESS

- Click the fourth button to register the entered values. The corresponding text output box confirms the registered values and reports the actual effective system NA, maximum allowed FOV (1D), and beam offset required to obtain the desired tilt.

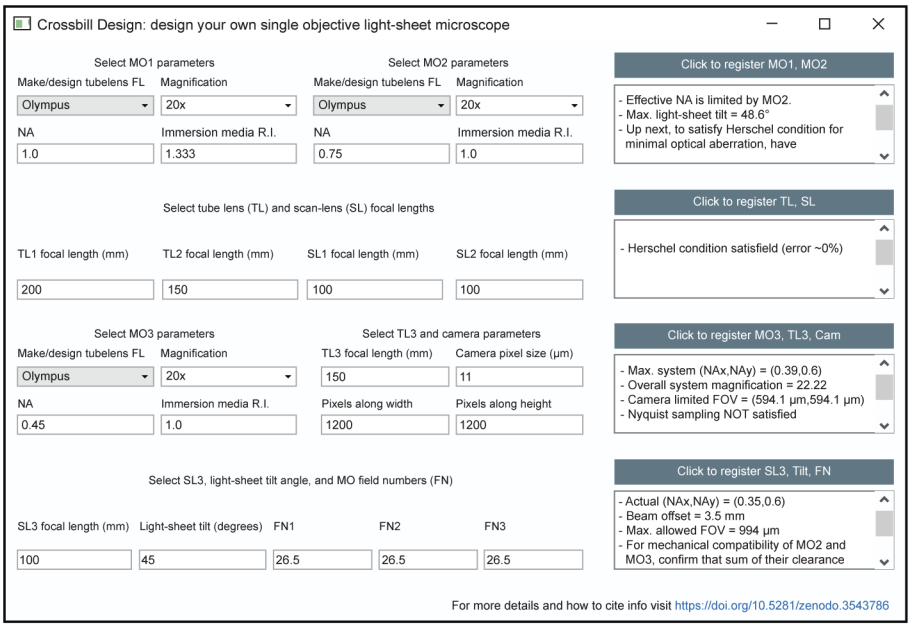

Fig. 8. An open source graphical user interface for optical parts selection in single objective light-sheet microscopy.

If the outcome parameters are not satisfactory, the user can go back and edit selections, and re-register them to see corresponding changes to the microscopy system. Clicking a button simulates all previous button clicks. For the user's convenience, the fourth and final button click also logs all the design parameters and corresponding results in a text file, along with a system timestamp. This text file (CrossbillDesign_summary.txt) is written in the same parent folder where the code is running.

Funding

National Institute of Mental Health (R01MH117111); Arnold and Mabel Beckman Foundation (Beckman Young Investigator Award); Kinship Foundation (Searle Scholar Award); Rita Allen Foundation (Rita Allen Scholar Award).

Disclosures

MK and YK are authors of a patent filed for SOPi microscopy.

References

1. H. Siedentopf and R. Zsigmondy, "Uber sichtbarmachung und größenbestimmung ultramikoskopischer teilchen, mit besonderer anwendung auf goldrubingläser," Ann. Phys. **315**(1), 1–39 (1902).
2. A. H. Voie, D. Burns, and F. Spelman, "Orthogonal-plane fluorescence optical sectioning: Three-dimensional imaging of macroscopic biological specimens," J. Microsc. **170**(3), 229–236 (1993).
3. Y. Wu, A. Ghitani, R. Christensen, A. Santella, Z. Du, G. Rondeau, Z. Bao, D. Colón-Ramos, and H. Shroff, "Inverted selective plane illumination microscopy (ispim) enables coupled cell identity lineaging and neurodevelopmental imaging in caenorhabditis elegans," Proc. Natl. Acad. Sci. **108**(43), 17708–17713 (2011).

Biomedical Optics EXPRESS

4. Y. Wu, P. Wawrzusin, J. Senseney, R. S. Fischer, R. Christensen, A. Santella, A. G. York, P. W. Winter, C. M. Waterman, Z. Bao, D. A. Colón-Ramos, Z. McAuliffe, and H. Schroff, "Spatially isotropic four-dimensional imaging with dual-view plane illumination microscopy," Nat. Biotechnol. **31**(11), 1032–1038 (2013).
5. T. F. Holekamp, D. Turaga, and T. E. Holy, "Fast three-dimensional fluorescence imaging of activity in neural populations by objective-coupled planar illumination microscopy," Neuron **57**(5), 661–672 (2008).
6. M. Tokunaga, N. Imamoto, and K. Sakata-Sogawa, "Highly inclined thin illumination enables clear single-molecule imaging in cells," Nat. Methods **5**(2), 159–161 (2008).
7. B. Migliori, M. S. Datta, C. Dupre, M. C. Apak, S. Asano, R. Gao, E. S. Boyden, O. Hermanson, R. Yuste, and R. Tomer, "Light sheet theta microscopy for rapid high-resolution imaging of large biological samples," BMC Biol. **16**(1), 57 (2018).
8. A. K. Glaser, N. P. Reder, Y. Chen, C. Yin, L. Wei, S. Kang, L. A. Barner, W. Xie, E. F. McCarty, C. Mao, A. R. Halpern, C. R. Stoltzfus, J. S. Daniels, M. Y. Gerner, P. R. Nicovich, J. C. Vaughan, L. D. True, and J. T. C. Liu, "Multi-immersion open-top light-sheet microscope for high-throughput imaging of cleared tissues," Nat. Commun. **10**(1), 2781 (2019).
9. C. Dunsby, "Optically sectioned imaging by oblique plane microscopy," Opt. Express **16**(25), 20306–20316 (2008).
10. E. J. Botcherby, R. Juskaitis, M. J. Booth, and T. Wilson, "Aberration-free optical refocusing in high numerical aperture microscopy," Opt. Lett. **32**(14), 2007 (2007).
11. E. J. Botcherby, R. Juškaitis, M. J. Booth, and T. Wilson, "An optical technique for remote focusing in microscopy," Opt. Commun. **281**(4), 880–887 (2008).
12. J. Huisken, J. Swoger, F. Del Bene, J. Wittbrodt, and E. H. Stelzer, "Optical sectioning deep inside live embryos by selective plane illumination microscopy," Science **305**(5686), 1007–1009 (2004).
13. S. Kumar, D. Wilding, M. B. Sikkel, A. R. Lyon, K. T. MacLeod, and C. Dunsby, "High-speed 2d and 3d fluorescence microscopy of cardiac myocytes," Opt. Express **19**(15), 13839–13847 (2011).
14. M. B. Sikkel, S. Kumar, V. Maioli, C. Rowlands, F. Gordon, S. E. Harding, A. R. Lyon, K. T. MacLeod, and C. Dunsby, "High speed scmos-based oblique plane microscopy applied to the study of calcium dynamics in cardiac myocytes," J. Biophotonics **9**(3), 311–323 (2016).
15. M. B. Bouchard, V. Voleti, C. S. Mendes, C. Lacefield, W. B. Grueber, R. S. Mann, R. M. Bruno, and E. M. Hillman, "Swept confocally-aligned planar excitation (scape) microscopy for high-speed volumetric imaging of behaving organisms," Nat. Photonics **9**(2), 113–119 (2015).
16. Y. Shin, D. Kim, and H.-S. Kwon, "Oblique scanning 2-photon light-sheet fluorescence microscopy for rapid volumetric imaging," J. Biophotonics **11**(5), e201700270 (2018).
17. M. Kumar, S. Kishore, J. Nasenbeny, D. L. McLean, and Y. Kozorovitskiy, "Integrated one-and two-photon scanned oblique plane illumination (sopi) microscopy for rapid volumetric imaging," Opt. Express **26**(10), 13027–13041 (2018).
18. M. Kumar and Y. Kozorovitskiy, "Tilt-invariant scanned oblique plane illumination microscopy for large-scale volumetric imaging," Opt. Lett. **44**(7), 1706–1709 (2019).
19. B. Yang, X. Chen, Y. Wang, S. Feng, V. Pessino, N. Stuurman, N. H. Cho, K. W. Cheng, S. J. Lord, L. Xu, D. Xie, R. Dyche Mullins, M. Leonetti, and B. Huang, "Epi-illumination spim for volumetric imaging with high spatial-temporal resolution," Nat. Methods **16**(6), 501–504 (2019).
20. M. Hoffmann and B. Judkewitz, "Diffractive oblique plane microscopy," Optica **6**(9), 1166–1170 (2019).
21. V. Voleti, K. B. Patel, W. Li, C. P. Campos, S. Bharadwaj, H. Yu, C. Ford, M. J. Casper, R. W. Yan, W. Liang, C. Wen, K. D. Kimura, K. L. Targoff, and E. M. C. Hillman, "Real-time volumetric microscopy of in vivo dynamics and large-scale samples with scape 2.0," Nat. Methods **16**(10), 1054–1062 (2019).
22. M. Born and E. Wolf, *Principles of Optics: Electromagnetic Theory of Propagation, Interference and Diffraction of Light* (Elsevier, 2013).
23. R. E. Fischer, B. Tadic-Galeb, and P. R. Yoder, *Optical System Design* (SPIE Press, 2008).
24. J. W. Goodman, *Introduction to Fourier Optics* (Roberts and Company Publishers, 2005).
25. V. N. Mahajan, *Aberration Theory Made Simple* (SPIE Press, 1991).
26. A. Millett-Sikking and A. York, "High numerical aperture single objective light-sheet," Zenodo (2019), https://doi.org/10.5281/zenodo.3244420.
27. M. Kumar and Y. Kozorovitskiy, "Crossbill design," Zenodo (2019), https://doi.org/10.5281/zenodo.3543786.